A Bayesian Classification Model for Sea Ice Roughness from Scatterometer Data

Markku Similä, Elja Arjas, Marko Mäkynen, *Member, IEEE*, and Martti T. Hallikainen, *Fellow, IEEE*

Abstract—For sea ice in the Baltic Sea, surface scattering can be regarded as the dominant scattering mechanism at C-band. In this paper, a new statistical method is introduced for making statistical inferences about the underlying ice surface roughness on the basis of one-dimensional (1-D) scatterometer data y. The central parameter in the hierarchical model applied in the context is a mixture parameter p, which indicates the degree of surface roughness in ice surface. Several questions related to the occurrence of different ice classes on a transect can be solved with the aid of the posterior distribution $[p|y]$. An empirical approximation for the posterior distribution is computed by using Markov Chain Monte Carlo methodology. The efficiency of the suggested approach is investigated by analyzing a C-band HH-polarization helicopter-borne HUTSCAT scatterometer data. The results provided by the statistical model show good agreement with a video-based ice type classification.

Index Terms—C-band radar, hierarchical models, Markov Chain Monte Carlo, scatterometer, sea ice, surface roughness.

I. Introduction

THE BALTIC Sea is a brackish water area that belongs to the seasonal ice zone. The relatively thin ice cover is in a continuous motion and undergoes deformation due to winds and currents. This leads to a large variability in the severity and in the thickness of the resulting deformed ice fields. Deformed ice has a rough surface topography that appears as ice ridges and rubble fields. The width of ridges usually ranges from one to a few meters. Identification of a single ridge from satellite SAR images is highly uncertain if the data are acquired in a mode that enables a wide spatial coverage (like the 50-m resolution for the RADARSAT ScanSAR narrow mode). The blurred appearance of ridged areas in a SAR image entails that the identification of ice fields cannot be easily converted into a classification problem with geophysically interpretable results. This can be contrasted with the fact that for winter ship navigation the single most important task is to locate the most ridged ice areas.

Several backscatter modeling studies have been conducted in order to understand the interaction of radar waves in the low-salinity Baltic sea ice [1]–[3]. Although important advances have been made in this area, they have not resulted in a reliably functioning ice-type identification algorithm. On the other hand, the development of the classification methods utilizing image data has suffered from the lack of detailed ground truth data sets. The evaluation of the results is based on the visual interpretation of SAR scenes and on the information given on the ice charts (resolution from 5 to 10 km) of the Finnish Ice Service [4]. This assessment procedure is uncertain if one aspires to extract detailed knowledge about the ice mass distribution of the ice cover. One can appreciate the degree of uncertainty in this assessment method by reading our account about the coherence between two separate visual interpretations of the same video imagery in Section II. The most extensive radar data set with a good field validation over the Baltic sea ice has been acquired by the HUTSCAT C- and X-band scatterometer (nonimaging radar) [5] from 1992 to 1997 involving a simultaneous synchronized video recording (see Section II). The scatterometer produces very accurate backscattering measurements along a line crossing an ice field.

Surface scattering can be regarded as the dominant scattering mechanism for the C-band data set analyzed here (see Section III-A). Hence, one may aim to reconstruct the ice surface that generated the measured backscatter. The main emphasis in this paper lies on the introduction of a new statistical method to make statistical inferences for the underlying ice surface roughness, i.e., to solve statistically the stated ice surface reconstruction problem. A restriction of the analysis performed here is that the field validation procedure using video imagery (see Section II) allows us to make only qualitative statements concerning surface roughness.

A model-based approach for the surface reconstruction problem is adopted that is methodologically close to the nonparametric estimation method proposed in [6]. The statistical inference is focused on a mixture parameter p, which has a clear geophysical interpretation in the model, see Section III. An approximation for the posterior distribution of p given the data is computed by using Markov Chain Monte Carlo methodology. During the simulation, a large sample from the posterior distribution is drawn. Many quantities and estimates of interest can be computed from these as Monte Carlo averages. With the aid of the posterior distribution one can find an answer, e.g., to the following questions.

1) What is the most likely ice class label at a particular site?
2) How certain is it that the class label in question is correct?
3) What is the total length of the line segments belonging to a particular ice class that are encountered when traveling along a specified transect, and what is the uncertainty of the estimate?

4) When traveling along a specified transect, how many highly deformed ice areas with a diameter exceeding, for instance, 1 km need to be crossed, and what is the uncertainty of the estimate?

Usually, in segmentation problems, the focus is on questions of the first type. The Bayesian framework adopted here allows us to answer the other types of questions as well. As far as we know, problems such as 3 and 4 from the list, although of considerable importance in practice, have not been previously discussed in the sea ice remote sensing literature. The accuracy of the given answers will naturally depend on both the data and on the model assumed.

II. HUTSCAT DATA SET

The measurement instruments are presented here together with the ice classes applied. This is because the selection of ice types was dictated by the capability to correctly identify the different ice types, which again depended on the instrumentation that was used.

A. HUTSCAT Measurements

Backscattering signatures of various Baltic Sea ice types have been measured with the helicopterborne C- and X-band (5.4 and 9.8 GHz) HUTSCAT scatterometer during six ice research campaigns from 1992 to 1997 [7]. Here we consider only the data acquired in March 1997 at C-band HH-polarization (equivalent to RADARSAT SAR) at an incidence angle of 23°. At the time of the measuring the weather was cold (mean air temperature from −11 °C to −7 °C) and the very thin snow cover on the ice was dry. The overall length of the measurement test lines is about 65 km, resulting in 2587 pixels when the data are averaged to the resolution of 25 m. Several factors influenced the choice of this resolution: 1) satellite SAR images can be acquired at this resolution; 2) the standard deviation of the fading in a single backscattering coefficient (σ^o) is negligible, below 0.4 dB [7], and thus the consecutive values represent very well true spatial variation of the target; and 3) the strong spatial variation characteristic to ridged areas is still present. The test lines were imaged by a synchronized video recorder. Hence, it was possible to assign for each pixel an ice type based on a visual assessment.

B. Ice Types

The Baltic Sea ice cover is rather thin (mean thickness usually less than 70 cm), but its extent and severity vary strongly both locally and annually [8]. Variation of the surface roughness of the Baltic Sea ice is quite large. Newly formed ice is very smooth and with time, the surface roughness grows by the action of mechanical deformation in an ice field, i.e., rafting (thin ice) or ridging (thick ice) and thermal deformation due to changing weather conditions (temperature, wind, snow). The largest discontinuities in the ice surface roughness are created by the occurrence of ice ridges that are thick but long and narrow accumulations of ice blocks with sail height typically less than 2 m. The width of an ice ridge varies strongly but is usually of a

magnitude of a few meters. The density of the occurrence of ice ridges has a large spatial variation [9], [10].

The ice-type classification used here is based on mutual discussions with the Finnish Ice Service. The goal was to find ice classes that would be informative for the winter ship traffic but still identifiable from the video imagery. The HUTSCAT data were classified into five different ice types, see Table I and Fig. 1. The ice field was first divided into two main ice types, level ice and deformed ice. The level ice class was divided further into three ice classes: new ice, smooth level ice, and rough level ice. New ice is a general term for ice that is only a few days old. It does not pose any difficulties for ship traffic. Smooth level ice is almost unaffected by deformation, only cracking or finger rafting may occur. Rough level ice has protruding ice blocks and floe edges and low uneven surface areas and it has typically broken one or more times and frozen again. The level ice types are no obstacles for the ice breakers but, depending on ice thickness, they can slow down or even block navigation of low ice class ships. Distinguishing between three different level ice subtypes is probably not necessary from a ship navigation point of view, but backscattering signatures of these subtypes are different due to their different surface roughness (see Fig. 1). Slightly deformed ice consists of ice ridges, uneven surfaces, and level ice areas, whose sizes are usually larger than the pixel size in operatively used SAR imagery (100 m). The average size of level ice areas in highly deformed ice is usually smaller than the pixel size and the proportion of level ice areas is smaller than in slightly deformed ice, i.e., the degree of deformation is higher. Slightly deformed ice tends to slow down or block ship navigation. Highly deformed ice areas may even block icebreaker navigation and they are usually avoided by all ships. Frozen brash fields, also called rubble fields, were originally selected as one ice type for the study. However, their backscattering signature could not be distinguished from that of highly deformed ice. Hence, this ice type was also labeled as being highly deformed. From a ship navigation point of view this is usually their proper classification.

In the visual classification of ice types from the video imagery, it was required that the segments representing an ice class should be at least ten pixels (250 m) long. The choice of the ice type becomes more realistic when the ice field is considered over a reasonable area. However, discrimination of slightly deformed ice from highly deformed ice is difficult and introduces a strong subjective component into the classification. Different analysts performing video classification would typically report slightly different classification results. The author responsible for the visual classification repeated his video-based classification for the three test lines analyzed here one year later. The consistency of the resulting classifications with the original classifications were 78%, 87%, and 98%, depending on the test line. The main differences were that some areas that had earlier been interpreted as being highly deformed were now considered as only slightly deformed, and some that had previously been interpreted as slightly deformed ice were now considered as rough level ice or as unidentified ice. Finally, in some cases, previously unidentified ice types were now classified as rough level ice.

It should be noted that the HUTSCAT data set consists of more measurements over highly deformed ice area than what
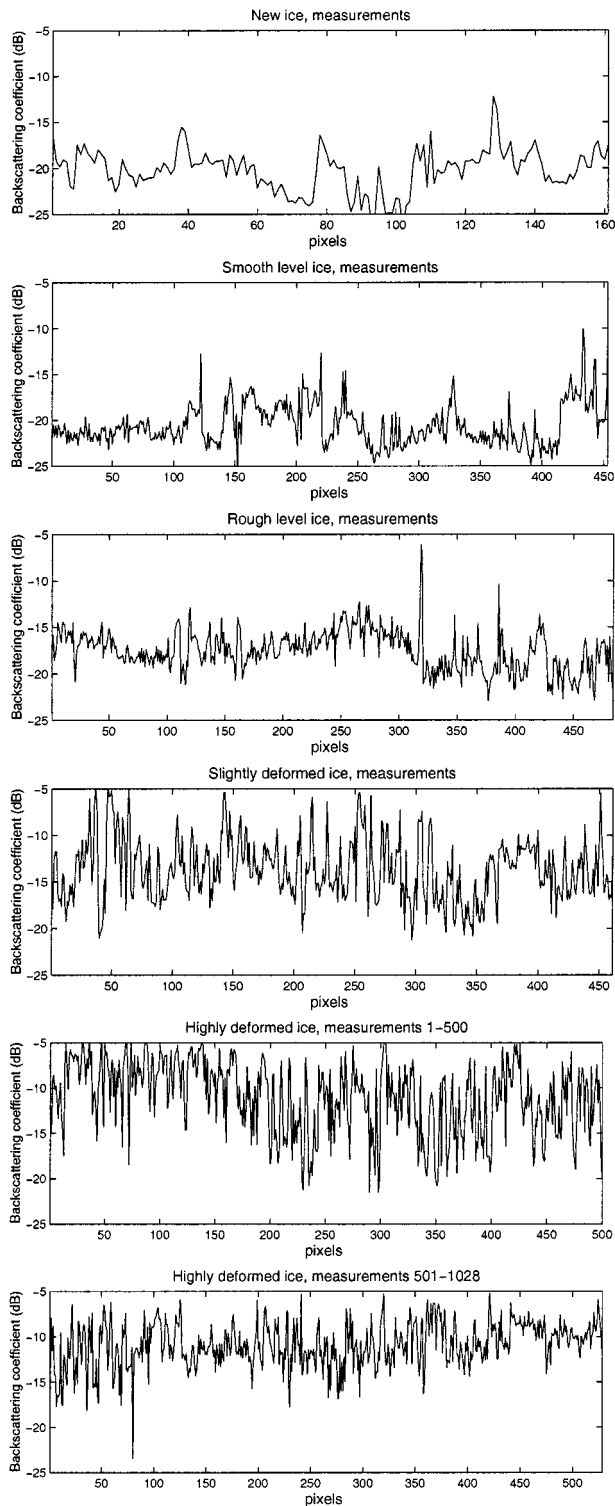
Fig. 1. Scatterometer measurements for new ice (class 1), smooth level ice (class 2), rough level ice (class 3), slightly deformed ice (class 4), and highly deformed ice (class 5).

TABLE I
ICE CLASSES USED IN THE VISUAL INTERPRETATION

Ice type	Class index	Number of pixels
new ice	1	161
smooth level ice	2	453
rough level ice	3	484
slightly deformed ice	4	461
highly deformed ice	5	1028
Total		2587

III. HIERARCHICAL MODEL FOR SIGNAL VARIATION

A. The Physical Interpretation of the Model

In backscatter modeling, analytic expressions are used to describe backscattering from a target with known properties. One of the most widely applied models is the integral equation model (IEM) [11]. It contains the following parameters: standard deviation of the ice surface height statistics, ice surface autocorrelation function, dielectric constant, incidence angle, radar wave number, and radar wave polarization. In our data set, all three radar parameters were kept fixed. The weather was cold and the measured ice fields were physically close to each other. Hence, the variation of the dielectric constant of the ice and the effect of the snow layer can be assumed to be small. Since surface scattering is assumed to be the dominant scattering mechanism at C-band for co-polarized measurements in the Baltic Sea ice at the incidence angle that was used [1], [3], the changes in the ice surface roughness are regarded as the main source of the observed backscatter intensity fluctuation in the data set.

In all radar measurements the surface roughness is considered against the radar wavelength (here 5.7 cm). For example, in the IEM model, the small-scale surface roughness condition is $ks < 2$, where k is radar wavenumber, and s is surface root mean square (RMS) roughness. For the data set of interest here, this means that the standard deviation of a surface height profile (RMS roughness) should be less than 1.8 cm. RMS values below this threshold are reported for the Baltic Sea when the length of the profile is 1 m [12]. Using the radar wavelength as a scaling unit, we found it useful to decompose the surface roughness into small-scale and large-scale components, in spite of the fact that the exact discrimination between these scales is somewhat diffuse. The large-scale surface roughness in the Baltic Sea ice is controlled primarily by the amount and the sizes of ice ridges. A schematic description of these roughness scales is shown in Fig. 2.

In the data set, the backscattering coefficients have a wide dynamic range, from values close to the noise floor of the HUTSCAT scatterometer (−25 dB) to the value of −5 dB. Note that in the following we will use mostly the word "signal" to refer to the measured backscattering coefficient.

The statistics (both the mean and the variance) for level ice areas and deformed ice areas deviate from each other significantly (see Fig. 1). In the case of level ice areas, the average value increases due to the increase of the surface roughness but,

are commonly encountered in the Baltic Sea (see Table I). Many test lines were chosen over these ice fields because they constitute the most severe problem for the ship navigation. A part of the test lines (approximately 23%) did not get any ice type identification and they were discarded from the statistical analysis. Usually, the abandoned test line part consisted of mixtures of several different ice types.
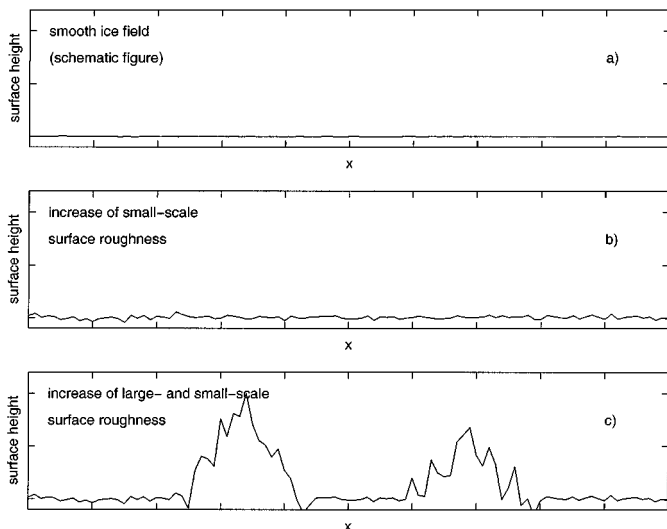
Fig. 2. (a) Smooth ice fields have the smallest surface roughness. The surface roughness (b) increases due to thermal variation or (c) due to simultaneous mechanical deformation. Manninen [12] obtained RMS heights ranging from 0.2 cm to 1.5 cm when the profile length was 1 m (small-scale variation). The sail height of a single ice ridge is mostly below 2 m in the Baltic Sea [9]. The mean number of ridges per km varies strongly, typical values being from 0 to 10 ridges per km (large-scale variation).

interestingly enough, the classwise variances remained about the same in all three level ice classes.

Occasionally, in level ice fields, there occur spikes, mostly upwards. These spikes (symmetric with respect to the radar travelling direction) are most likely generated by an ice floe edge or some other morphological deformation appearing in the ice surface.

Characteristic of the behavior of the measured signal over the deformed ice areas is that both the mean and the variance of the signal values increase significantly when compared to level ice classes (see Fig. 1). The magnitude of the signal oscillation in deformed ice areas is critically dependent on the spatial resolution. At the 25 m resolution used here, the variances of the deformed ice classes are about twice as large as for level ice classes. The signal fluctuation over deformed ice areas arises because the amount, the orientation, and the size of the ice blocks of a ridge inside a resolution cell vary from one pixel to another. Signal variation does not, however, unambiguously grow as a function of the mean signal power. For some highly deformed ice fields, as in the measurements 590–640 in Fig. 1, the backscattered power remains for a long time on a relatively high level and the signal variation is small.

The variation in ice surface roughness and its relation to signal variation suggest an approach where one assigns different stochastic processes to surfaces with a small and to surfaces with a large height variation.

For this purpose, consider a measured signal from an ice surface with a small surface height variation. Let random variables $U = (U_i)$ denote the pixelwise values associated with this kind of scattering. These variables are modeled as a stochastic process with low mean and relatively heavy tails. The heavy tails assumption allows the range of measurement values to be large, as was the case with the data obtained.

Suppose then that the backscattered signal is generated by a highly deformed ice area. Random variables $V = (V_i)$, which denote pixelwise values related to this scattering, constitute a stochastic process with a high mean value and heavy tails. Notice that the process V models backscattering over units (pixels), which consist of a collection of ridges with different widths and heights, and no explicit assumptions are made about the backscattering behavior of a single ridge.

We assign to the mean of the process U a value low enough (-22 dB) so that a measured signal less than this mean can be taken as a clear indication of new ice or smooth level ice. Correspondingly, the mean of the process V is chosen to be high enough (-8 dB) so that a measured signal above this value would typically arise only from a highly deformed ice field. Fig. 1 shows that only few exceptions to these rules can be found in the data set. In our model the resulting pointwise posterior mean and median (see Sections III-B and IV) were restricted on the interval $(-22, -8)$.

The adopted approach is based on the following simplified description of an ice surface. A transect along an ice surface consists of intervals of level ice separated by ice ridges. The more densely the ridges are spaced, the more deformed the ice field. We assume that all ice fields can be described by varying only the ridging intensity, i.e., the number of ridges per unit interval. The variation of the ridging density is expressed in our approach by regarding each ice field as a mixture of two extreme ice types, smooth level ice and heavily ridged ice. We write the measured backscattering coefficient Y over a pixel in an arbitrary ice field as

$$Y = (1-p)U + pV, \qquad \text{where } p \in (0, 1). \qquad (1)$$

To be able to utilize the proposed mixture approach one has to consider a collection of pixels simultaneously. This requirement is fulfilled because each ice field is made up of several consecutive pixels (see Section II). The motivation for selecting the simple abstraction described in (1) is the fact that only qualitative assessments about the underlying ice surface roughness are at our disposal and that the mixture approach enables us to model the observed features in the data in an easily interpretable manner.

As we already remarked, the given verbal description of an ice field as a scattering surface ignores many aspects that are present in the data. First, the effect of the volume scattering is ignored. Also, the backscattered power from a level ice area increases with increasing small-scale surface roughness independently of the possible occurrence of ridges. This is illustrated in Fig. 1, when moving from ice class 2 to ice class 3. In this case, p in (1) increases. This is in agreement with our classification goal because then the mean ice thickness also usually increases. In addition to ice ridges, also other large-scale features appear on the ice surface, namely, rubble fields. However, both these morphological features are results of alternating converge/divergence movements that drift ice fields continuously undergo, and both features indicate accumulation of ice mass. The given description ignores also the size of a single ice ridge although this has an effect in the decision of whether the ice field

in question should be considered slightly or highly deformed. The ridge size is partially reflected in the strength of backscattering because large ridges increase the surface roughness more than small ones. Finally, the orientation of an ice ridge with respect to the radar viewing angle has some effect on the backscattering strength [13], [14].

Despite the deficiencies caused by the simplifications, we shall utilize the above mixture model in the statistical analysis. In the Bayesian approach adopted here, statistical inference concerning the ice types will be expressed in terms of conditional probabilities assigned to the values of the parameters $p = (p_i)$ given the observed data y. To facilitate such statistical inference, a hierarchical model is provided with the aim of computing an approximative posterior distribution $[p|y]$.

B. Hierarchical Model

Let $y = (y_1, \ldots, y_n)$ denote the measurements along the transect. Bayesian inference about the unknown parameters $\Theta = (\theta_1, \ldots, \theta_r)$ in a statistical model is based on the posterior distribution $[\Theta|y] \propto [y|\Theta][\Theta]$, where $[y|\Theta]$ is the likelihood function, and $[\Theta]$ is the prior distribution for the model parameters. Here the notation $[a|b]$ generically denotes the conditional density of a given b. Similarly, $[a]$ denotes the (marginal) density of a.

We shall make some assumptions concerning the structural properties of the components in the parameter vector Θ. This is realized through hyperparameters γ that influence the observations y only through the parameters Θ. In this case, it is true for the posterior distribution that $[\Theta, \gamma|y] \propto [y|\Theta][\Theta, \gamma]$, see [15].

The following parameters are included in our model: the intensity λ of a controlling Poisson process, a point pattern ξ generated by the Poisson process, marks p^* associated to the points ξ, and the variances (σ_U^2, σ_V^2) of the processes U and V [see (1)]. By applying the chain rule repeatedly and by taking into account the conditional independencies between the parameters in our model, the posterior density turns out to be proportional to the following product ($\theta = (p^*, \sigma_U^2, \sigma_V^2)$):

$$[\theta, \xi|y, \lambda] \propto [\xi|\lambda][p^*|\xi][\sigma_V^2][\sigma_U^2|\sigma_V^2][y|p^*, \sigma_U^2, \sigma_V^2]. \quad (2)$$

Let us start the more detailed specification of the model mentioned previously by describing the simulation of the point pattern ξ and the corresponding marks p^*. First, we generate a point pattern $\xi = (\xi_1, \ldots, \xi_K)$ on the line segment I and denote by $\Delta_k(\xi)$ the intervals that arise when I is broken into subintervals separated by the points in ξ. The use of Voronoi tessellations as in [6] would have been an alternative to this. The prior distribution of the point pattern ξ is chosen to be the homogeneous Poisson process on I with a given intensity λ, $\lambda > 0$. For a pattern ξ with K points, the prior density $p(\xi)$ with regard to the unit intensity Poisson process is then proportional to $\lambda^K e^{-\lambda|I|}$.

The prior distribution of the marks $p^* = (p_1^*, \ldots, p_K^*)$ is developed conditionally on the unmarked pattern ξ. Given a pattern ξ with K points, the conditional density $[p^*|\xi]$ over the K intervals is defined to be simply the product

$$[p^*|\xi] = \prod_{k=1}^{K} [p_k^*] \quad (3)$$

where the marks p_k^* are independent and identically distributed [here $[p_k^*] \sim U(0, 1)$, see (4)].

In the previous section, the measured backscattering was expressed in terms of a convex combination of two indepent scattering processes U and V. We assign fixed values to the pair (x_U, x_V), which represents the mean values of the processes U and V. The means can be regarded as hyperparameters of the model. Their values [see (4)] are selected on the basis of our understanding of what values would be applicable for this data set and for the instrument that was used. For other data sets, one can choose another pair of values based on the prior knowledge of the ice conditions and their backscatter signatures.

The distribution of the pair of variances (σ_U^2, σ_V^2) is defined jointly. This specification depends naturally on the resolution of the data. At the 25 m resolution, the signal variance of the whole data set was about 24 dB. As we have attributed this variation to two independent processes, we can assume that both these processes have a variance smaller than the overall variance of the signal. It is also natural to assume that the variance σ_U^2 associated with the scattering from a smooth surface is smaller than the variance σ_V^2 associated with the scattering from a surface with a large height variation. We actually require that this be true for all samples simulated from the posterior distribution. This requirement is fulfilled if $[\sigma_V^2]$ and $[\sigma_U^2|\sigma_V^2]$ in (2) are chosen as follows. The (marginal) density of σ_V^2 is assumed to be uniform on the interval (c_1, c_2), where c_1 and c_2 are some given constants, and the fraction that σ_U^2 constitutes from σ_V^2 is taken to be Beta-distributed. Hence, both the joint prior and posterior distributions are supported by the triangle $T = \{(\sigma_U^2, \sigma_V^2): c_1 \leq \sigma_V^2 \leq c_2, c_1 \leq \sigma_U^2 \leq \sigma_V^2\}$. The small amount of noise present in the signal is included in the variances of the scattering processes.

We are now ready to specify a hierarchical model for the analysis of the data. The model summarizes all the different aspects discussed previously (subscript notation: i = index of a pixel, j = index of the random interval Δ_j such that $i \in \Delta_j$)

$$\lambda = 0.01,$$
$$x_U = -22,$$
$$x_V = -8,$$
$$[\sigma_V^2] \sim U(4, 20),$$
$$[\sigma_U^2|\sigma_V^2] \sim Beta(3, 3) \times \sigma_V^2,$$
$$[p_j^*] \sim U(0, 1),$$
$$\gamma_j^2 = (1 - p_j^*)\sigma_U^2 + p_j^*\sigma_V^2,$$
$$\mu_j = (1 - p_j^*)x_U + p_j^*x_V,$$
$$[y_i|\mu_j, \gamma_j^2] \sim N(\mu_j, \gamma_j^2). \quad (4)$$

On the highest level of the hierarchy, the intensity λ of the Poisson process is given. This controls how many fine random partitions one considers during the computations. On the lowest level of the hierarchy is the distribution of a single measurement given the parameters and their structural properties. The joint distribution of measurements is given later in (5). The mixture

parameter is used both in the definition of the local mean and of the local variance.

During the visual interpretation, the entire transect line I to be analyzed was partitioned into disjoint intervals (Δ_j) and to each interval Δ_j was assigned one of the five possible ice class labels (see Section II). It was required that each such interval should include at least ten pixels. Hence, also the estimated class label of some particular interval should be decided by examining the joint distribution of the measurements. This spatial continuity requirement is incorporated into model (4) by keeping p_j^* fixed on each random segment Δ_j. The fixed value of p_j^* is also consistent with our way of defining the ice type through the value of the mixture parameter [see (1)].

To complete the specification of the hierarchical model we assume that the measurements y_{ij} are independent given the partition and the parameters. Since $I = \cup_k \Delta_k(\xi)$, the joint likelihood for all measurements is given by

$$[y|\xi, p^*, \sigma_U^2, \sigma_V^2] = \prod_{j=1}^{K} \prod_{i \in \Delta_j} [y_i|\mu_j, \gamma_j] \qquad (5)$$

where each $[y_i|\mu_j, \gamma_j]$ is as in (4).

An essential ingredient in the computation of the model (4) is the random partition of the line into random segments. Hence, the approach adopted here is a variant of the nonparametric Bayesian estimation procedure developed by Arjas and Heikkinen [6], [16], which utilizes the reversible jump Markov Chain Monte Carlo method of Green [17]. In this approach, the dimension of the parameter space varies, it may increase (birth move) or decrease (death move).

To draw samples from the joint posterior of the model parameters, we used a single-site updating Metropolis–Hastings–Green algorithm where the acceptance probability $prob_B$ for the birth proposal can be written

$$\text{prob}_B = \min\{1, A\}$$

where $A =$ (posterio ratio) $\times$ (proposal ratio) $\times$ (Jacobian). For the death proposal, the acceptance probability is $\min\{1, A^{-1}\}$.

To implement the proposed hierarchical model, the reader should have some familiarity with the MCMC algorithms. A good introduction with several applications is [19]. Several aspects relating to our implementation are described in [20].

IV. RESULTS

The model has two distinctive features. On one hand, the variance of the signal values is assumed to increase as the ice class becomes more deformed. On the other hand, ice classes have a spatial continuity property, in the sense that several consecutive pixels in the analyzed transect belong to the same ice class. In the hierarchical model (4), these features were incorporated by utilizing the mixture parameter vector p^* in the parameterization and by imposing order restrictions on the pair of variances.

We base the statistical inference on the empirical posterior distribution $[p|y]$, where $p = (p_1, \ldots, p_n)$, $n = \#|I|$, and y is the given data (p_i refers to the value of the mixture parameter in the pixel i and p_k^* refers to the mixture parameter of the

random segment Δ_k). In the analysis, we will focus exclusively on posterior quantities, although the condition "given the data" is not always explicitly denoted. We define an auxiliary variable $z_i = (1 - p_i) \times x_U + p_i \times x_V$, where x_U and x_V are the same as in the model (4). This variable takes values on the interval (x_U, x_V). We use the pointwise posterior median $Med[z_i|y]$ as a summary statistic of the distribution $[z_i|y]$, computing it from the samples drawn from the posterior distribution during the simulation. Another possibility would have been to use the pointwise posterior mean $E[z_i|y]$. In our experiments, the posterior medians and means differed only slightly. Due to its robust character, the pointwise posterior median gave somewhat better results and hence, it was preferred.

Plotting the original measurements together with the pointwise posterior median along the transect, and in parallel with the visual classification, the following observations can be made (see Fig. 3). The median $Med[z_i|y]$ stays almost constant or changes very smoothly inside most segments. When one comes to a change point where an ice class changes to another according to the visual interpretation, these changes are usually accompanied by jumps in the level of the median $Med[z_i|y]$. In some segments the posterior median undergoes strong and abrupt variations (e.g., pixels 1000–1150 in Fig. 3). These fluctuations arise when the signal values are exceptionally low or high (with respect to the mean intensity level of the segment in question) for a relatively long time. This kind of behavior can hardly be avoided unless smoothing (depending on the parameter λ) is so strong that short segments can no longer be detected.

To examine further the classwise behavior of the pointwise posterior median, we computed for each ice class the histograms using both the original signal values and the pointwise posterior medians, see Fig. 4. This figure illustrates the important property of $Med[z_i|y]$, in that its values are concentrated on much narrower intervals than the original signals.

The results displayed in Fig. 4 are based on a MCMC simulation of 20 000 iterations, with a burn-in phase of 2000 iterations. The parameters were saved after every 250 iterations. By construction, the Metropolis–Hastings–Green sampler has the posterior distribution as its stationary distribution. However, the question arises whether the summaries based on the simulated samples are actually representative, i.e., does the empirical posterior distribution approximate well the theoretical posterior distribution. The samples from the posterior variances (σ_U, σ_V) produced by the MCMC procedure were examined with the aid of the CODA program [18]. In view of the Geweke, Heidelberger–Welch, and autocorrelation diagnostic tests, the burn-in phase was long enough and the mixing of the sampler was deemed to be satisfactory.

The results obtained here for the pointwise posterior median suggest that one can successfully use this statistic as a discriminant in the ice-type classification problem. This idea was tested by the following experiment. A new simulation with the same amount of iterations as before was run utilizing only the measurements of pixels 1–1400. A comparison between the visual classification and the empirical values of $Med[z_i|y]$ was performed, and a set of thresholds was determined to discriminate the different ice types. Then a new simulation with the measurements of pixels 1401–2587 was performed. The number of
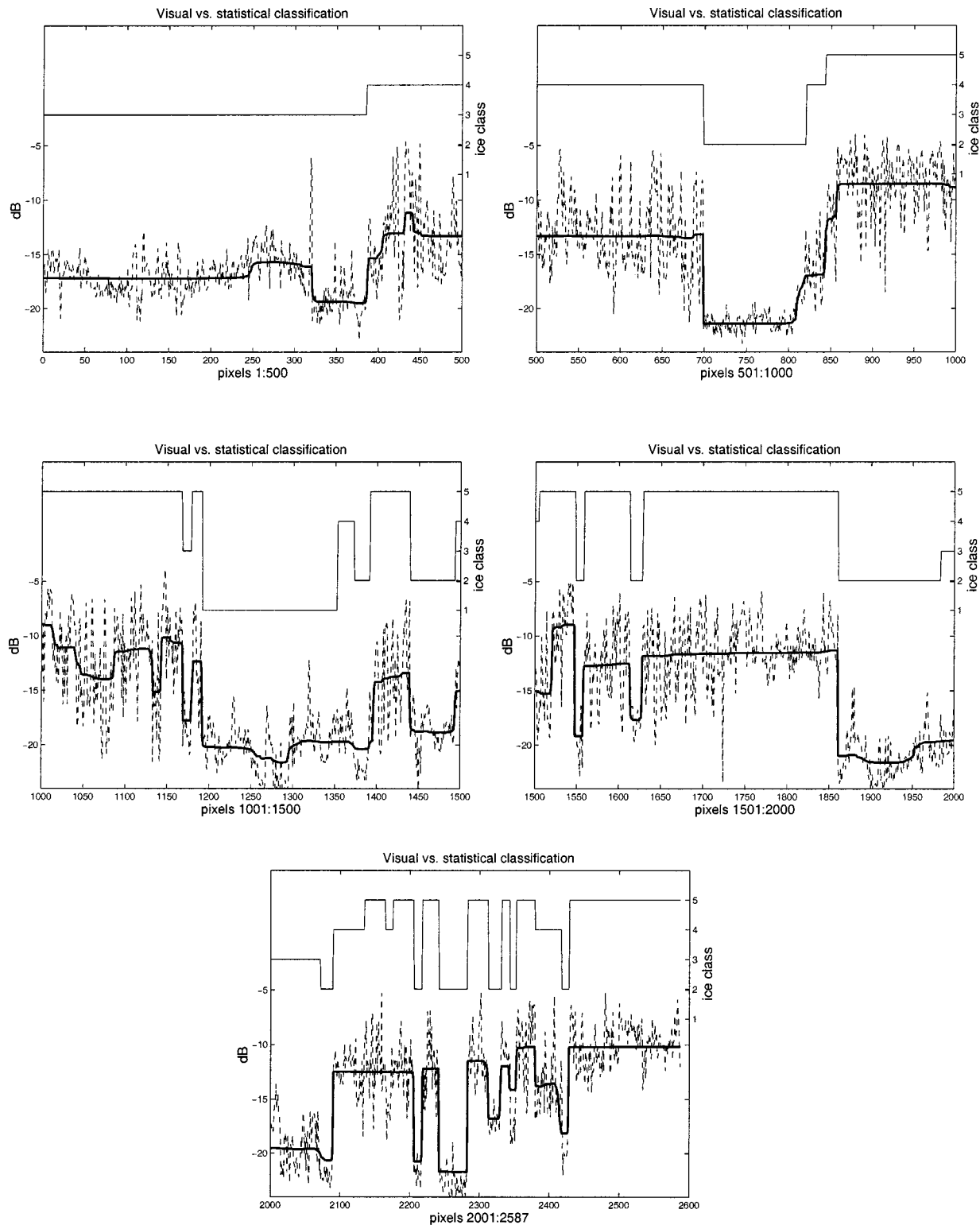
Fig. 3. Estimated pointwise posterior median (thick line) is drawn among the measurements (dashed line). The results of the visual assessment are displayed in the upper part of each figure with the same class indices as in Table I.

iterations was kept the same. For this data set, the ice classes given by the visual classification and those based on the pointwise posterior median agreed in 85% of the pixels. In this experiment the ice classes 1 (new ice) and 2 (smooth level ice) were combined because they can not be discriminated on the basis of $Med[z_i|y]$.

Correct identification of highly deformed ice areas is of great practical importance. We note that 91% of pixels on the latter half of the interval (pixels 1401–2587) that were regarded to represent highly deformed ice fields according to the visual classification were assigned to the same ice class by the pointwise posterior median in the second simulation. However, in addition
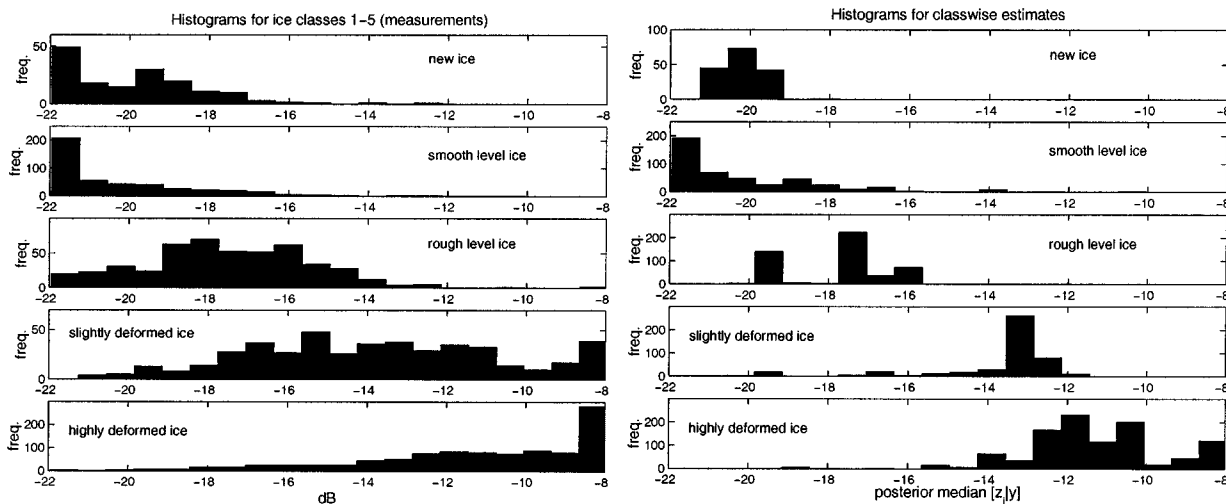
Fig. 4. Histograms of the measured backscattering coefficients and the pointwise posterior medians for new ice (class 1), smooth level ice (class 2), rough level ice (class 3), slightly deformed ice (class 4), and highly deformed ice (class 5).
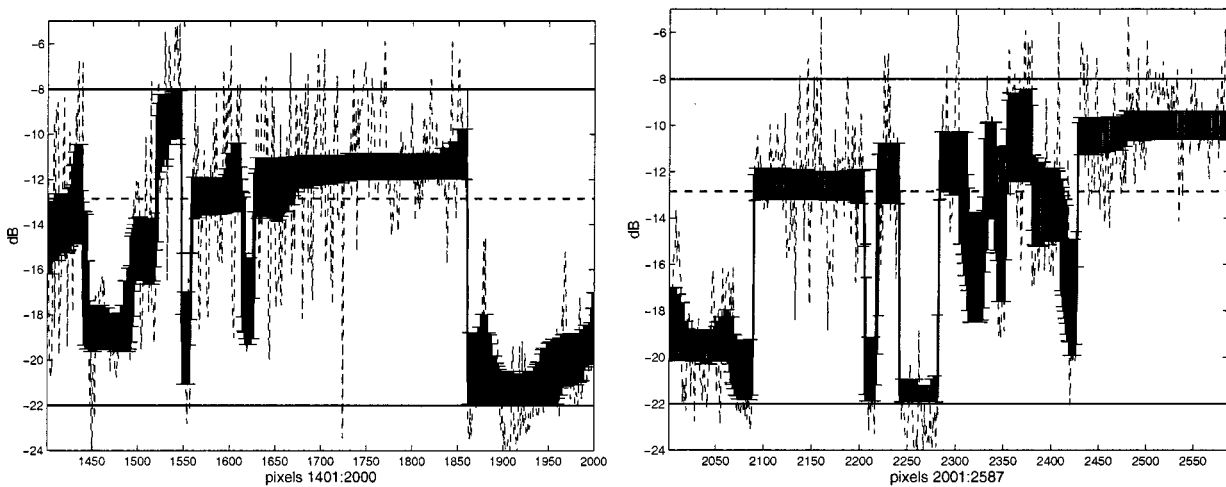

Fig. 5. Quantile intervals (0.05, 0.95) of the pointwise empirical posterior distributions $[z_i|y]$ are displayed (the dark band among the measurements). Measurements are represented with a thin dashed line. The thick dashed line at -12.85 dB is the threshold between highly deformed ice field and smoother ice areas (for details, see text).

to assigning class labels one can make also other statistical conclusions from the same empirical posterior distribution.

The following questions were examined.

1) What is the total length of the line segments belonging to highly deformed ice class that are encountered in the latter part of the transect (pixels 1401–2587), and what is the uncertainty of the estimate?
2) In the previous situation, how many continuous highly deformed ice fields are there in which the diameter along the transect exceeds 1 km?
3) In the previous situation, what is the diameter along the transect of the longest continuous highly deformed ice field?

These kind of questions are motivated by the fact that the spatially large highly deformed ice fields constitute the worst obstacles for winter ship traffic, see Section II-B.

The answers to these questions were derived simply by applying to each posterior sample the previously computed

threshold (-12.85 dB) between highly deformed ice areas and smoother ice surfaces. The results were (see Fig. 5) as follows.

1) The posterior median estimate for the total length was 16 775 m, and the 90% credibility interval was (13 200 m, 18 100 m). The uncertainty of the estimate (given the model and the data) was computed by using the 0.05 and 0.95 quantiles. The visual assessment arrived at the length of 17 050 m.
2) The posterior median estimate for the number of segments with the required property was four and the 90% credibility interval was [3, 6]. The visual assessment gave five such segments.
3) The posterior median estimate for the diameter was 5500 m and the 90% credibility interval was (3375 m, 5825 m). According to the visual assessment, the longest diameter was 5800 m.

To summarize, the estimates given by the model were in good agreement with the results of the visual assessment. Supposing that the visual assessments gave the "true" values,

our method slightly underestimated the area occupied by the highly deformed areas. However, the empirical credibility interval covered in all three cases the result given by the visual classification. Moreover, as the visual assessment carried a strong subjective component and its reliability was not perfect (see Section II-B), its results must be viewed with some caution.

We note that with these same tools one can tackle also other questions such as: "What is the probability (given the model and the data) that a highly deformed ice area with a diameter greater than c km is encountered?."

V. CONCLUSIONS

A model-based approach was applied for the identification of different ice types. It gave good results that are easy to interpret geophysically. The approach adopted here also enabled us to quantify probabilistically the uncertainty involved in the estimation, which greatly enhances practical decision making in the contex.

The proposed approach, based on piecewise constant functions, can be extended to SAR image data. Instead of considering transect lines and performing a classification of random intervals, one could perform a spatial analysis based on, for example, random triangles. By suitably restricting the set of permissible updates for triangles, this approach could be made computationally manageable. The knowledge about how scattering statistics depend on the incidence angle can be incorporated into the model in a flexible manner.

Two-dimensional (2-D) image data, unlike the one-dimensional (1-D) scatterometer data considered here, exhibits directional variation. Even though this variation may be strong, its duration is often quite short. This kind of directional variation is very typical for sea ice SAR images. The orientation information is not well captured by the local variance/covariance structure. Hence, it may be preferable to first apply a variance preserving transformation (e.g., the wavelet transform or the Gabor transform) that redistributes the total variance of the original data into new components that are ordered according to the orientation and the scale of the variation. Then an appropriate hierarchical model is built, and an analysis based on the statistical model is performed in the transform domain.

One of the restrictions in the analysis was that the ground truth data allowed only a qualitative assessment of the surface roughness. To obtain quantitative estimation results for the surface roughness one would need additional laser profilometer data, measured simultaneously with the scatterometer data.

In the estimation procedure, we utilized random partitions driven by the Poisson process with a prespecified intensity λ. If the value of λ is changed, the results given by the model change. The user must base the specification of the value of λ on his/her judgment as to what scale would be most appropriate for an investigation of the data of interest. Although the magnitude class of the smoothing parameter is crucial, the results are not highly sensitive to the actual value used. The intensity used here was 0.01, corresponding to the expected length of 2500 m for a random segment. However, the intensity values on the interval (0.005, 0.02), corresponding to expected lengths in (5000 m, 1250 m) for a random segment, gave very similar results.

REFERENCES

[1] A. Carlström and L. M. H. Ulander, "Validation of backscatter models for level and deformed ice sea ice in ERS-1 SAR images," *Int. J. Remote Sensing*, vol. 16, no. 7, pp. 3245–3266, 1995.

[2] T. Manninen, "Microwave surface backscattering and surface roughness of Baltic Sea ice," in *Finnish Marine Res.*. Helsinki, Finland: Finnish Inst. Marine Res., 1996.

[3] W. Dierking, M. I. Pettersson, and J. Askne, "Multifrequency scatterometer measurements of Baltic Sea ice during EMAC-94/95," *Int. J. Remote Sensing*, vol. 20, no. 2, pp. 349–372, 1999.

[4] M. Similä and J. Karvonen, "Classification of first-year sea ice using pulse-coupled neural network," in *Information Processing for Remote Sensing*, C. H. Chen, Ed. Singapore: World Scientific, 1999, pp. 295–316.

[5] M. Hallikainen, J. Hyyppä, J. Haapanen, T. Tares, P. Ahola, J. Pulliainen, and M. Toikka, "A helicopter-borne eight-channel ranging scatterometer for remote sensing—Part I: System description," *IEEE Trans. Geosci. Remote Sensing*, vol. 31, pp. 161–169, Jan. 1993.

[6] E. Arjas and J. Heikkinen, "An algorithm for nonparametric Bayesian estimation of a Poisson intensity," *Comput. Statist.*, vol. 12, no. 3, pp. 385–402, 1997.

[7] M. Mäkynen and M. Hallikainen, "Investigation of C- and X-band backscattering signatures of the Baltic Sea ice," *IEEE Trans. Geosci. Remote Sensing*, to be published.

[8] A. Seinä and E. Palosuo, "The classification of the maximum annual extent of ice cover in the Baltic Sea 1720–1995," *MERI-Rep. Series Finnish Inst. Marine Res.*, vol. 27, pp. 79–91, 1996.

[9] J. E. Lewis, M. Leppäranta, and H. B. Granberg, "Statistical properties of sea ice surface topography in the Baltic Sea," *Tellus*, vol. 45A, pp. 217–142, 1993.

[10] M. Lensu, "Laser profilometer measurements in the Bay of Bothnia during the ZIP-97 Experiment," Ship Lab. Rep. Series M-232, Helsinki Univ. Technol., Espoo, Finland, 1998.

[11] A. K. Fung, *Microwave Scattering and Emission Models and their Applications*. Norwood, MA: Artech House, 1994.

[12] T. Manninen, "Surface roughness of Baltic Sea ice," *J. Geophys. Res.*, vol. 102, no. C1, pp. 1119–1139, 1997.

[13] R. Johansson, "Detection and characterization of ice ridges in the Baltic Sea using CV-580 SAR imagery," in *Proc. Int. Geoscience and Remote Sensing Symp.'89*, Vancouver, BC, Canada, 1989, pp. 386–389.

[14] J. Hyyppä and M. Hallikainen, "Classification of low-salinity sea ice types by ranging scatterometer," *Int. J. Remote Sensing*, vol. 13, no. 13, pp. 2399–2413, 1992.

[15] A. Gelman, J. B. Carlin, H. S. Stern, and D. B. Rubin, *Bayesian Data Analysis*. London, U.K.: Chapman & Hall, 1995.

[16] J. Heikkinen and E. Arjas, "Non-parametric Bayesian estimation of a spatial Poisson intensity," *Scan. J. Statist.*, vol. 25, pp. 435–450, 1998.

[17] P. J. Green, "Reversible jump Markov chain Monte Carlo computation and Bayesian model determination," *Biometrika*, vol. 82, pp. 711–732, 1995.

[18] N. G. Best, M. K. Cowles, and S. K. Vines, "CODA manual, v. 0.30," MRC Biostatistics Unit, Inst. Public Health, Cambridge, U.K., 1996.

[19] W. R. Gilks, S. Richardson, and D. J. Spiegelhalter, *Markov Chain Monte Carlo in Practice*. London, U.K.: Chapman & Hall, 1996.

[20] M. Similá. (2000) The implementation of the MCMC algorithm to analyze scatterometer data. [Online]. Available: www.rni.helsinki.fi/~mhs

Markku Similä received the M.S. degree in mathematics from the University of Helsinki, Helsinki, Finland, in 1982.

Since 1990, he has been a Research Scientist at the Finnish Institute of Marine Research, Helsinki, Finland, where his research has concentrated on sea ice SAR images. His research interests are in statistical interpretation models for remote sensing radar data and analysis of images through different mathematical representations.

Elja Arjas received the Ph.D. degree in applied mathematics from the University of Helsinki, Helsinki, Finland, in 1972.

He is currently a Professor of Biometry at the Rolf Nevanlinna Institute, University of Helsinki, and a Research Professor with the National Public Health Institute (KTL), Finland. His main research interests are in Bayesian statistical inference with an emphasis on hierarchical and nonparametric modeling. He is currently joint Editor of the *International Statistical Review*.

Dr. Arjas is a Fellow of the Institute of Mathematical Statistics and a member of the International Statistical Institute.

Marko Mäkynen (S'87–M'95) received the Lic.Sci.Tech. degree from the Department of Electrical and Communications Engineering, Helsinki University of Technology (HUT), Helsinki, Finland, in 1999, where he is currently pursuing the Ph.D. degree in electrical engineering.

He is currently a Senior Teaching Assistant in the Laboratory of Space Technology, HUT. His research interests are microwave remote sensing of sea ice and calibration of scatterometers.

Martti T. Hallikainen (M'83–SM'85–F'93) received the M.Sc. degree in engineering and the Dir.Tech. degree from the Helsinki University of Technology (HUT), Faculty of Electrical Engineering, Espoo, Finland, in 1971 and 1980, respectively.

Since 1987, he has been Professor of Space Technology, HUT, where his research interests include remote sensing and satellite technology. In 1988, he established the HUT Laboratory of Space Technology and serves as its Director. He was a Visiting Scientist from 1993 to 1994 at the European Union's Joint Research Centre, Institute for Remote Sensing Applications, Ispra, Italy. He was a Postdoctoral Fellow with the Remote Sensing Laboratory, University of Kansas, Lawrence, from 1981 to 1983, and was awarded an ASLA Fulbright Scholarship with the University of Texas, Austin in 1974–1975.

Dr. Hallikainen served as President of IEEE Geoscience and Remote Sensing Society (IEEE GRSS) in 1996 and 1997, and as Vice President in 1994 and 1995. Since 1988, he has been a member of the IEEE GRSS Administrative Committee and since 1999, he has served as IEEE GRSS Nominations Committee Chair. He was General Chairman of the IGARSS'91 Symposium and Guest Editor of the Special IGARSS'91 Issue of the IEEE TRANSACTIONS ON GEOSCIENCE AND REMOTE SENSING (TGARS). Since 1992, he has been an Associate Editor of TGARS. He was a member of the IEEE Periodicals Committee in 1997 and corresponding member of the IEEE New Technology Directions Committee from 1992 to 1995. He was Secretary General of the European Association of Remote Sensing Laboratories (EARSeL) from 1989 to 1993 and Chairman of the Organizing Committee for the EARSeL 1989 General Assembly and Symposium. He has been a member of EARSeL Council since 1985 and he was member of the Editorial Board of the EARSeL Advances in Remote Sensing from 1992 to 1993. He has been a member of the European Space Agency's (ESA) Earth Science Advisory Committee since 1998 and a member of ESA SMOS Scientific Advisory Group since 2000. He was a national delegate to the ESA Earth Observation Scientific and Technical Advisory Group (EOSTAG) from 1988 to 1994, and he has served in the same capacity on the ESA Earth Observation Data Operations Scientific and Technical Advisory Group (DOSTAG) since 1995. He was Thematic Coordinator of the ESA EMAC-95 airborne campaign for Snow and Ice activities. He was a member of the ESA Multi-frequency Imaging Microwave Radiometer (MIMR) Expert Group from 1988 to 1994 and a member of the ESA MIMR Scientific Advisory Group from 1994 to 1996. He has been a member of the Advisory Committee for the European Microwave Signature Laboratory of the European Union's Joint Research Centre since 1992 and the National Liaison of the International Space University since 1992. He has served as Commission F Vice Chair of the International Union of Radio Science (URSI) from 1999 to 2002. He was a member of the URSI Long Range Planning Committee from 1996 to 1999, official member of URSI Commission F (Wave Propagation and Remote Sensing) since 1988, a member of the URSI Committee on Geosphere and Biosphere Program from 1989 to 1999 and URSI representative to SCOR since 1999. He was Secretary of the Organizing Committee for the URSI Nordic Antenna Symposium in 1976, and he served as Secretary of the Finnish National Committee of URSI from 1975 to 1989. He was Vice Chairman of the URSI Finnish National Committee from 1990 to 1996, and he has served as Chairman since 1997. He has been Vice Chair of the Finnish National Committee of COSPAR since 2000. He is the recipient of three IEEE GRSS Awards: 1999 Distinguished Achievement Award, IGARSS'96 Interactive Paper Award, and 1994 Outstanding Service Award. He was the winner of the Microwave Prize for best paper in the 1992 European Microwave Conference and received the HUT Foundation Award for excellence in research in 1990. He and his research team received the 1989 National Research Project of the Year Award from *Tekniikka & Talous* (*Technology & Management Magazine*). He also received the 1984 Editorial Board Prize of Sähkö—Electricity in Finland.